ACS APPLIED MATERIALS & INTERFACES

www.acsami.org Research Article

# Thickness-Independent Semiconducting-to-Metallic Conversion in Wafer-Scale Two-Dimensional $PtSe_2$ Layers by Plasma-Driven Chalcogen Defect Engineering

Mashiyat Sumaiya Shawkat,△ Jaeyoung Gil,△ Sang Sub Han, Tae-Jun Ko, Mengjing Wang, Durjoy Dev, Junyoung Kwon, Gwan-Hyoung Lee, Kyu Hwan Oh, Hee-Suk Chung, Tania Roy, YounJoon Jung,* and Yeonwoong Jung*

Cite This: *ACS Appl. Mater. Interfaces* 2020, 12, 14341−14351 Read Online

ACCESS | Metrics & More | Article Recommendations | Supporting Information

**ABSTRACT:** Platinum diselenide ($PtSe_2$) is an emerging class of two-dimensional (2D) transition-metal dichalcogenide (TMD) crystals recently gaining substantial interest, owing to its extraordinary properties absent in conventional 2D TMD layers. Most interestingly, it exhibits a thickness-dependent semiconducting-to-metallic transition, i.e., thick 2D $PtSe_2$ layers, which are intrinsically metallic, become semiconducting with their thickness reduced below a certain point. Realizing both semiconducting and metallic phases within identical 2D $PtSe_2$ layers in a spatially well-controlled manner offers unprecedented opportunities toward atomically thin tailored electronic junctions, unattainable with conventional materials. In this study, beyond this thickness-dependent intrinsic semiconducting-to-metallic transition of 2D $PtSe_2$ layers, we demonstrate that controlled plasma irradiation can "externally" achieve such tunable carrier transports. We grew wafer-scale very thin (a few nm) 2D $PtSe_2$ layers by a chemical vapor deposition (CVD) method and confirmed their intrinsic semiconducting properties. We then irradiated the material with argon (Ar) plasma, which was intended to make it more semiconducting by thickness reduction. Surprisingly, we discovered a reversed transition of semiconducting to metallic, which is opposite to the prediction concerning their intrinsic thickness-dependent carrier transports. Through extensive structural and chemical characterization, we identified that the plasma irradiation introduces a large concentration of near-atomic defects and selenium (Se) vacancies in initially stoichiometric 2D $PtSe_2$ layers. Furthermore, we performed density functional theory (DFT) calculations and clarified that the band-gap energy of such defective 2D $PtSe_2$ layers gradually decreases with increasing defect concentration and dimensions, accompanying a large number of midgap energy states. This corroborative experimental and theoretical study decisively verifies the fundamental mechanism for this externally controlled semiconducting-to-metallic transition in large-area CVD-grown 2D $PtSe_2$ layers, greatly broadening their versatility for futuristic electronics.

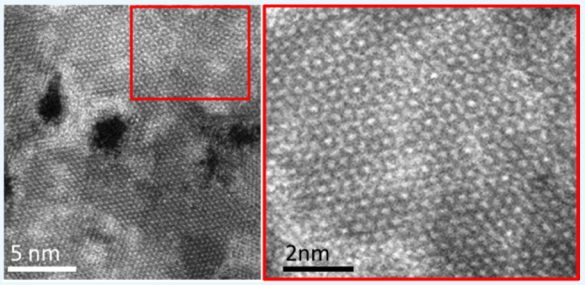


**KEYWORDS:** *2D TMD, 2D $PtSe_2$, wafer-scale 2D layer, plasma irradiation, semiconducting-to-metallic transition, defects engineering, DFT*



## INTRODUCTION

Two-dimensional (2D) transition-metal dichalcogenide (TMD) layers in the form of $MX_2$ (M: transition metals, X: chalcogens) exhibit a large set of extraordinary electrical properties such as thickness-tunable electron transport and band-gap energies.[1−11] Earlier works have focused on exploring semiconducting 2D TMDs, where M is generally group six refractory metals [e.g., molybdenum (Mo) or tungsten (W)], which are particularly suitable as channels in digital electronics. Increasing interest in the field has shifted investigation toward non-semiconducting 2D TMDs, projecting vast opportunities for other device components such as atomically thin interconnects and dielectrics. Recently, 2D TMDs employing group 10 noble metals [e.g., M = platinum (Pt) or palladium (Pd)] are receiving significant attention owing to various attributes unavailable in conventional semiconducting counterparts.[12,13] Among them, 2D platinum diselenide (2D $PtSe_2$) layers exhibit multifaceted extraordinary electrical properties, significantly higher field-effect transistor (FET) mobility than Mo- or W-based 2D TMDs, superior air stability, type II Dirac topological transitions, and thickness-dependent semiconducting-to-metallic tunability.[14−24] Furthermore, recent studies have verified defect-induced magnetism and its layer thickness

Received: January 3, 2020
Accepted: March 3, 2020
Published: March 3, 2020




https://dx.doi.org/10.1021/acsami.0c00116
*ACS Appl. Mater. Interfaces* 2020, 12, 14341−14351

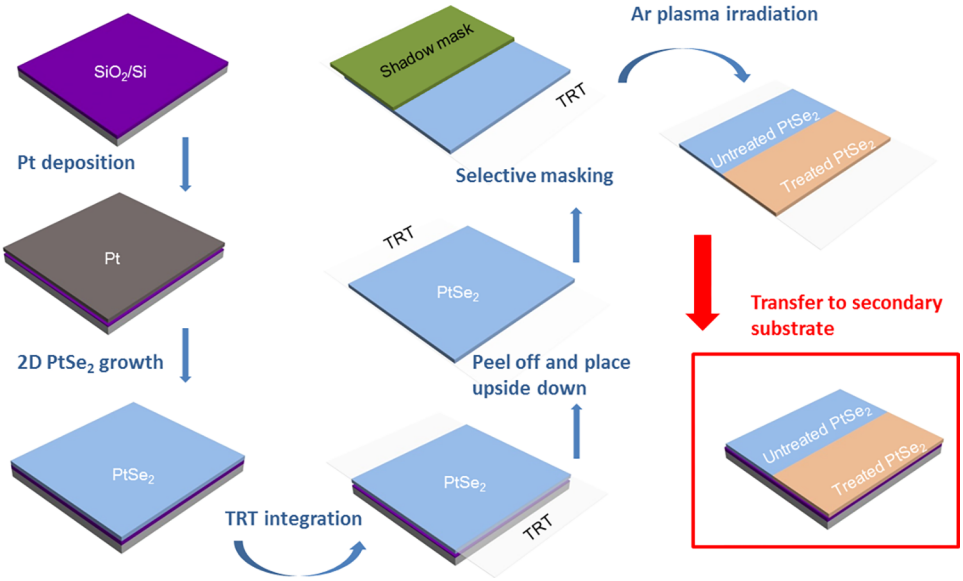


**Figure 1.** Schematic illustration for the preparation of Ar-plasma-treated and -untreated areas within identical 2D $PtSe_2$ layers.

dependency, indicating unprecedented promise in spintronics as well.[25] These unique yet superior properties suggest unparalleled promise for developing atomically thin circuitry with tailored electronic junctions. For instance, the co-existence of semiconducting and metallic phases within identical 2D $PtSe_2$ layers can realize in-plane, atomically thin Schottky junctions,[26] unlike other 2D heterostructures based on laterally stitching layers of distinct compositions.[27,28] Accordingly, a variety of proof-of-concept applications have been approached including sensing,[29−31] thermoelectrics,[32,33] and broad-band photodetection and photovoltaics.[18,34−42] Among such promising attributes, the semiconducting-metallic phase tenability is an "intrinsic" feature of 2D $PtSe_2$ layers set by their intrinsic crystallinity, i.e., layer thickness and/or orientation, which is governed by their preparation methods such as chemical growth conditions[36] These distinguishable carrier transport characteristics are of particular interest for the contact engineering of 2D layers toward improving their Ohmic transports, i.e., atomically seamless Ohmic contacts within 2D layers.[43] Accordingly, it is highly demanded to develop postgrowth methods to "externally" modulate such features in a spatially defined and controlled manner, which will significantly broaden the application versatility of 2D $PtSe_2$ layers. In this endeavor, structural engineering such as controlling defect concentrations via physical/chemical means has been explored with conventional 2D TMD semiconductor layers including Mo or W disulfide ($MoS_2$ or $WS_2$) and diselenide ($MoSe_2$ or $WSe_2$).[44] Particularly, the atomic concentration of chalcogen vacancies is known to alter their electronic band structures, thereby resulting in carrier transport properties.[44,45] Theory suggests that a selective creation of chalcogen vacancies can contribute to forming unsaturated electrons surrounding transition metals acting as electron donors.[46] The prediction is consistent with recent experimental observations that corroborate the vacancy-driven closing of band-gap energies in 2D $WS_2$ and $WSe_2$ layers.[47] However, these approaches have been demonstrated with initially single-crystalline 2D flakes of small ($\sim\mu m^2$) lateral dimensions and inhomogeneous spatial distribution/coverage. Accordingly, they are practically limited toward realizing the aforementioned opportunities for atomically thin circuitry, which should rely on "wafer-scale" 2D layers produced by mass production routes such as chemical vapor deposition (CVD). It is highly demanded to develop scalable methods to externally and controllably fabricate both semiconducting and metallic phases within identical 2D layers toward the direct writing of wafer-scale circuitry. The feasibility of such defect engineering for modulating carrier transports in large-area (>$cm^2$) CVD-grown 2D $PtSe_2$, a relatively unexplored 2D material, with intrinsic polycrystallinity has remained largely unexplored.

In this report, we demonstrate controlled modulation of carrier transport properties in CVD-grown centimeter-scale 2D $PtSe_2$ layers via argon (Ar) plasma irradiation. Two-dimensional (2D) $PtSe_2$ layers are known to be metallic above a certain critical thickness (typically more than ~10 nm), below which they prefer to possess semiconducting properties.[48] We grew 2D $PtSe_2$ layers of very small (a few nanometer) thickness and confirmed their intrinsic semiconducting characteristics. We then applied a controlled Ar-plasma irradiation to them and investigated the resulting carrier transport properties. Unlike the conventional notion, which predicts more pronounced semiconducting characteristics, we observed that this plasma irradiation steadily introduces a semiconducting-to-metallic transition accompanying increasing conductivity, verified by FET and temperature-variant electrical measurements. By performing extensive chemical characterization including energy-dispersive X-ray spectroscopy (EDS) and X-ray photoelectron spectroscopy (XPS), we identified that after plasma treatment, the Pt/Se ratio changes from 1:2 to 1:$x$, where $x$ is ~1.1−1.25. Extensive [transmission electron microscopy (TEM)] characterization confirmed that these Se-deficient metallic 2D layers still preserved high polycrystallinity comparable to their pristine state without a noticeable reduction of initial thickness, exposing a large number of atomic vacancies on the surface. Density functional theory (DFT) calculations revealed that the plasma-induced creation of Se vacancies introduces various midgap energy states within 2D $PtSe_2$ layers toward closing their band-gap energy. Moreover, the extent of this band-gap energy closing


https://dx.doi.org/10.1021/acsami.0c00116
ACS Appl. Mater. Interfaces 2020, 12, 14341−14351

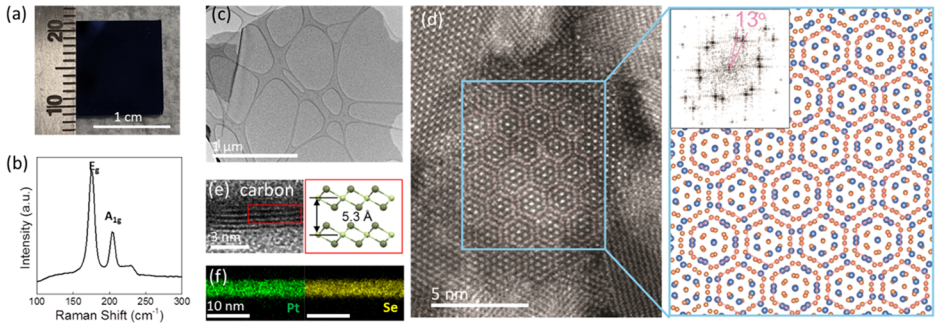


**Figure 2.** Structural and chemical characterization of as-grown 2D $PtSe_2$ layers. (a) Image of large-area 2D $PtSe_2$ layers grown on a $SiO_2$/Si substrate. (b) Raman spectroscopy profile from the corresponding sample. (c) Low-magnification plane-view TEM image. (d) Corresponding HR-STEM image revealing Moiré fringe patterns (blue box) and their corresponding atomic structure simulation (right). The inset shows the FFT image corresponding to the blue box, depicting a misalignment angle of 13°. (e) Cross-sectional HRTEM image (left) revealing horizontally aligned 2D $PtSe_2$ multilayers and their corresponding atomic structure model (right). (f) STEM-EDS elemental mapping images corresponding to (e), confirming the homogeneous spatial distribution of Pt and Se.

was identified to scale with the concentration and dimension of such vacancies, which fully accounts for the experimental observation.

## RESULTS AND DISCUSSION

Figure 1 illustrates the process steps employed in the CVD growth of 2D $PtSe_2$ layers and their partially selected Ar-plasma irradiation. A Pt film of ∼0.6 nm was deposited on a $SiO_2$/Si wafer by electron beam deposition (deposition rate: ∼0.1 Å/s), and it was then converted into 2D $PtSe_2$ layers via CVD selenization at 400 °C using the growth recipe developed in our laboratory.[36,48] The as-grown 2D $PtSe_2$ layers exhibit a highly uniform morphology and thickness, entirely covering the original growth wafer, to be verified in the next section. A thermal release tape (TRT) was subsequently attached to the surface of the as-grown 2D $PtSe_2$ layers, and care was taken to ensure that there were no gaps between the tape and the 2D layers. Subsequently, the sample of TRT/2D $PtSe_2$/$SiO_2$/Si was immersed in deionized water, similar to the procedure demonstrated with 2D $MoS_2$ layers,[49] and a mechanical force was exerted to peel off the stack of TRT/2D $PtSe_2$ from the growth substrate. The separated stack was flipped over, exposing the 2D $PtSe_2$ layers on the top surface. Next, the 2D $PtSe_2$ layers were partially covered with a stainless steel shadow mask and were exposed to mild Ar plasma for controlled duration times. Details for the plasma conditions are listed in Experimental Section. The partially plasma-treated sample was then transferred onto a fresh $SiO_2$/Si wafer, and the TRT was subsequently removed upon heating at 80 °C. As a result, a lateral junction containing both pristine and plasma-treated areas was realized within identical 2D $PtSe_2$ layers. The aim of performing the Ar-plasma irradiation onto the 2D $PtSe_2$ layers "separated" from their underlying $SiO_2$/Si growth wafers was to rule out any unwanted effects from the degradation of $SiO_2$ dielectric and metal contacts caused by the plasma irradiation. In fact, we have observed that "direct" Ar-plasma irradiation onto as-grown 2D $PtSe_2$/$SiO_2$/Si samples often leads to the degradation and instability of the underlying $SiO_2$ dielectric and $SiO_2$/metal contacts in electrical measurements.

Figure 2 shows the structural and chemical analyses of as-grown 2D $PtSe_2$ layers prior to the Ar-plasma treatment. Figure 2a presents an image of as-grown 2D $PtSe_2$ layers on a $SiO_2$/Si wafer with a size of >1 $cm^2$, prepared by the CVD selenization of an ∼0.6 nm thick Pt film. Figure 2b shows the Raman spectroscopy characteristic peaks from the corresponding sample, exhibiting two dominant peaks of $E_g$ at ∼175 $cm^{-1}$ and $A_{1g}$ at ∼205 $cm^{-1}$, corresponding to the in-plane and out-of-plane vibration modes of 2D $PtSe_2$ layers, respectively.[48] Figure 2c–f exhibits the TEM characterization of the corresponding sample, identifying the general structural and chemical integrity of CVD-grown 2D $PtSe_2$ layers. Figure 2c shows a plane-view TEM image of the sample at a low magnification, confirming the spatially continuous and homogenous film morphology. Figure 2d shows the corresponding high-resolution scanning TEM (HR-STEM) image and its analysis, revealing the detailed atomic-scale structure of the CVD 2D $PtSe_2$ layers. The left HR-STEM image reveals their intrinsic polycrystallinity contributed by multiple crystalline grains of various crystallographic orientations, i.e., a mixture of crystal lattice fringes resulting from (001) zone axis-oriented hexagonal 2D $PtSe_2$ along with Moiré fringe patterns (blue box) from misaligned crystalline domains, a decisive signature of vertical stacking of horizontally aligned 2D basal planes. The blue-boxed image presented in the right panel was obtained from an atomic simulation of horizontally stacked 2D $PtSe_2$ layers with a misorientation angle of 13°, which precisely matches the Moiré fringe patterns in the HR-STEM image. The fast Fourier transform (FFT) corresponding to the HR-STEM image presented as the inset further confirms the misorientation angle of 13°. Figure 2e presents a cross-sectional TEM image of the corresponding sample, revealing horizontally aligned 2D $PtSe_2$ layers with uniformly resolved van der Waals (vdW) gaps. The interlayer spacing of ∼5.3 Å (Pt-to-Pt distance) is identified, which matches the (001) planar distance of the hexagonal 2D $PtSe_2$ crystal illustrated in the atomic structure model in the right panel. Figure 2f reveals the STEM-EDS elemental map images corresponding to Figure 2e, unveiling the highly uniform distribution of constituting Pt and Se atoms.

Having confirmed the chemical and structural homogeneity of horizontally aligned 2D $PtSe_2$ multilayers (layer number: ∼4–5 in Figure 2e), we then characterized their electron transport properties via FET measurements. Layer-number-dependent semiconducting-to-metallic transitions in 2D $PtSe_2$ layers have been previously verified, e.g., a transition at 2D $PtSe_2$ of four to five layers,[22,23,50] while the exact layer numbers for such transitions vary in the literature,[15,17,26,51−53] which must be attributed to multiple variables associated with sample preparations. Two-dimensional (2D) $PtSe_2$ layer-based FET


https://dx.doi.org/10.1021/acsami.0c00116
ACS Appl. Mater. Interfaces 2020, 12, 14341−14351

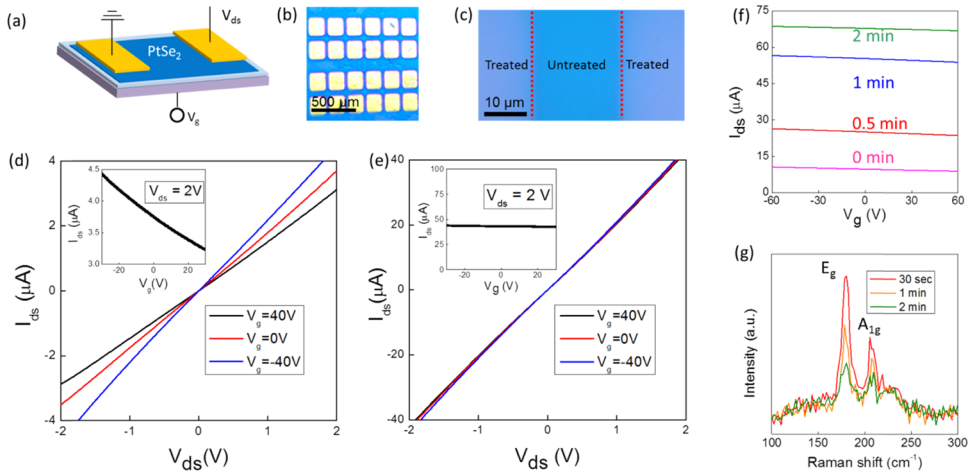


**Figure 3.** Electrical and Raman characterization of 2D $PtSe_2$ layers in their pristine and Ar-plasma-treated states. (a) Schematic of a 2D $PtSe_2$ layer-based FET device with Au electrodes in a back-gate configuration. (b) Optical microscopy image of a representative FET device. (c) Optical microscopy image unveiling color contrast between plasma-treated and -untreated regions within identical 2D $PtSe_2$ layers. (d) $I_{ds}-V_{ds}$ FET transfer plots from pristine 2D $PtSe_2$ layers, confirming p-type semiconducting characteristics. The inset shows the corresponding $I_{ds}-V_g$ transfer characteristics. (e) $I_{ds}-V_{ds}$ FET transfer plots from plasma-irradiated 2D $PtSe_2$ layers, confirming metallic characteristics with almost zero-gate modulation. The inset shows the corresponding $I_{ds}-V_g$ transfer characteristics. (f) $I_{ds}-V_{ds}$ characteristics from another FET device with thicker 2D $PtSe_2$ layers systematically irradiated with Ar-plasma for varying durations. The drain voltage was set at 1 V. (g) Raman spectroscopy profiles obtained from the sample corresponding to (f) with varying plasma irradiation times.

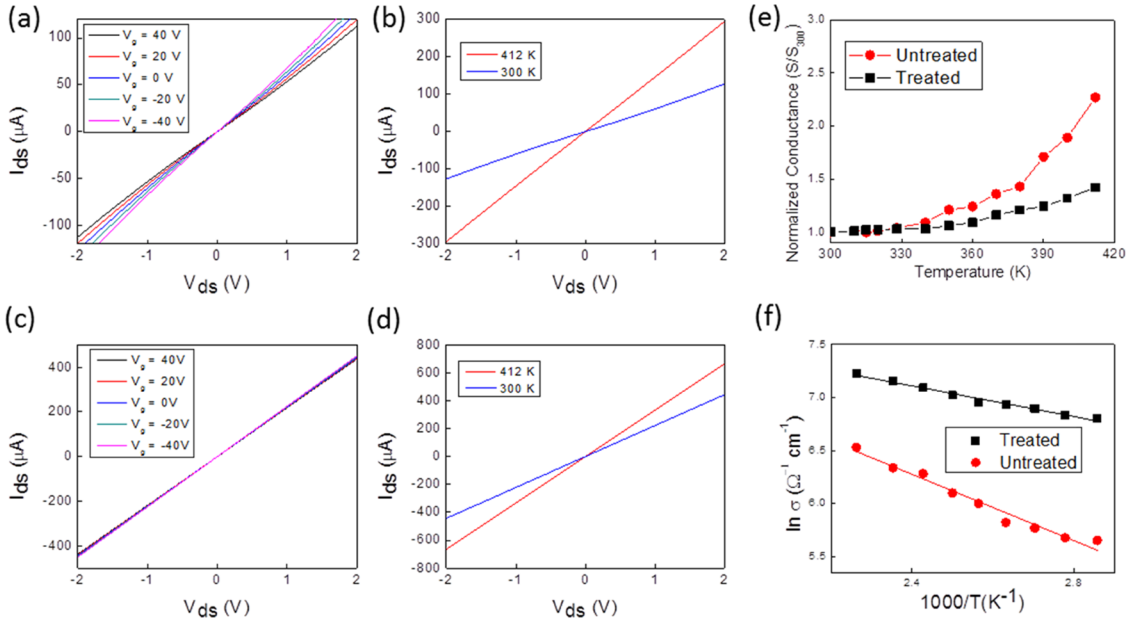


**Figure 4.** Temperature-variant FET transport characteristics of 2D $PtSe_2$ layers in pristine vs Ar-plasma-irradiated states. Pristine 2D $PtSe_2$ layers revealing (a) $V_g$-dependent $I_{ds}-V_{ds}$ transfer curves at 300 K and (b) $I_{ds}-V_{ds}$ characteristics under $V_g$ = 0 V obtained at 300 and 412 K. Ar-treated 2D $PtSe_2$ layers revealing (c) $V_g$-dependent $I_{ds}-V_{ds}$ transfer curves at 300 K and (d) $I_{ds}-V_{ds}$ characteristics under $V_g$ = 0 V obtained at 300 and 412 K. (e) Comparison of the current ratio with respect to 300 K as a function of temperature for the corresponding pristine and Ar-treated samples. (f) Comparison of activation energies for thermally driven transports of charge carriers in pristine vs Ar-plasma-treated 2D $PtSe_2$ layers.

devices were fabricated by depositing gold (Au) electrodes through a shadow mask onto the 2D $PtSe_2$ layers, which contain both pristine and Ar-plasma-treated areas, as prepared in Figure 1. Figure 3a illustrates a back-gated FET device with 2D $PtSe_2$ layers integrated on a fresh $SiO_2$/Si wafer, and Figure 3b shows an optical microscopy image of a representative device with an array of Au top electrodes. Figure 3c presents an optical microscopy image of 2D $PtSe_2$ layers with both Ar-plasma-treated vs untreated areas, revealing a slightly distinct optical contrast. Figure 3d,e exhibit the FET transfer characteristics of untreated and treated 2D $PtSe_2$ layers, respectively. Drain−source current ($I_{ds}$) vs drain−source voltage ($V_{ds}$) plots were obtained with varying amplitudes of back-gate voltage ($V_g$) for both. In Figure 3d, the pristine (i.e., untreated) 2D $PtSe_2$ layers display p-type semiconducting characteristics manifested by the decrease of $I_{ds}$ with increasing $V_g$ from −40 to 40 V, consistent with the $I_{ds}-V_g$ transfer plot in the inset. The result is in good agreement with the previous FET study with CVD 2D $PtSe_2$ layers of comparable thickness.[30,48] On the other hand, the 2D $PtSe_2$ layers treated



https://dx.doi.org/10.1021/acsami.0c00116
ACS Appl. Mater. Interfaces 2020, 12, 14341−14351

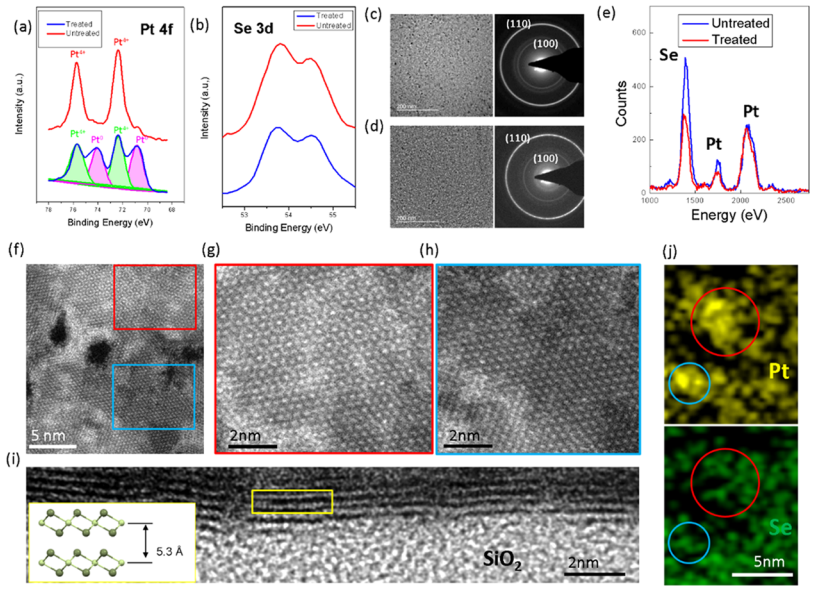


**Figure 5.** Structural and chemical characterization of 2D $PtSe_2$ layers before/after the Ar-plasma treatment. XPS spectra of (a) Pt 4f and (b) Se 3d core levels obtained from 2D $PtSe_2$ layers in pristine vs Ar-plasma-treated states. Low-magnification TEM images (left) and corresponding SAED patterns (right) from 2D $PtSe_2$ layers in (c) untreated and (d) treated states. (e) EDS spectra obtained from 2D $PtSe_2$ layers in Ar-plasma-treated and -untreated states. (f) HR-STEM image of Ar-plasma-irradiated 2D $PtSe_2$ layers. Zoom-in images corresponding to the (g) red and (h) blue boxes in (f). (i) Cross-sectional HRTEM image of Ar-plasma-irradiated 2D $PtSe_2$ layers. (j) EDS elemental map images visualizing a localized distribution of Pt and deficiency of Se.

with Ar plasma (duration time: 2 min in this case) display very distinct characteristics as presented in Figure 3e, i.e., the nearly complete overlap of $I_{ds}-V_{ds}$ plots irrespective of $V_g$ with increasing conductance, a signature of metallic transport. The corresponding $I_{ds}-V_g$ plot presented in the inset is also distinct from that in Figure 3d. This metallic behavior is quite interesting and unexpected, given that 2D $PtSe_2$ layers of such a small thickness (~3 nm as shown in Figure 2e) should belong to the semiconducting regime, as theoretically predicted and experimentally verified.[51,53] We also prepared 2D $PtSe_2$ layers by selenizing Pt films of a slightly larger thickness (~0.75 nm compared to ~0.6 nm in Figure 3a–e) and systematically identified their FET characteristics before/after the Ar-plasma treatment. Figure 3f presents $I_{ds}-V_g$ transfer plots of the corresponding 2D $PtSe_2$ layers, revealing a systematic increase of $I_{ds}$ with prolonged plasma treatment, which further confirms pronounced metallic properties. As mentioned in Figure 1, we have observed that the direct Ar-plasma irradiation onto fabricated $PtSe_2/SiO_2/Si$ FET devices leads to significantly increased leakage current in them. This indicates that the charge density state of underlying $SiO_2$ might have been significantly alternated by the plasma irradiation, leading to unstable (generally high) $I_{ds}$ even when $V_g = 0$ V, as presented in the Figure S1, Supporting Information. Figure 3g shows the Raman spectroscopy characterization of the identical 2D $PtSe_2$ layers prepared with varying Ar-plasma treatment times. While their relative peak intensity is observed to decrease systematically, it is evident that 2D $PtSe_2$ layers still well retain characteristic $E_g$ and $A_{1g}$ peaks even up to 2 min Ar-plasma treatment. A slight (~32%) broadening of the $E_g$ peak is noticed after the plasma treatment, which indicates a localized breaking of the crystal symmetry in 2D $PtSe_2$ layers, as previously reported.[54] Moreover, the plasma-induced decrease of both $E_g$ and $A_{1g}$ peak intensities is mainly attributed to the loss of Se atoms, to be verified in the next section. Additionally, we performed atomic force microscopy (AFM) characterization and confirmed that this mild Ar-plasma treatment does not significantly alter the overall thickness of 2D $PtSe_2$ layers. Corresponding AFM topography images and height measurement profiles, obtained from the samples different from those used for Figure 3, are presented in the Figure S2, Supporting Information.

Temperature-variant FET measurements were performed with both pristine and Ar-treated 2D $PtSe_2$ layers to gain insights toward better understanding the plasma-driven conversion of semiconducting-to-metallic transports. Figure 4a shows representative $I_{ds}-V_{ds}$ FET transfer curves from a sample of pristine 2D $PtSe_2$ layers with varying $V_g$ at 300 K. A clear gate modulation is observed, indicating its intrinsic semiconducting transport. Figure 4b presents $I_{ds}-V_{ds}$ FET transfer curves from the same sample under a fixed zero-gate bias (i.e., $V_g = 0$ V) at two different temperatures of 300 and 412 K. A significant (~2.3 times) increase of $I_{ds}$ is observed with increasing temperature by 112 K, which is a typical characteristic of temperature-dependent carrier transports in semiconducting crystals. Figure 4c shows $I_{ds}-V_{ds}$ FET transfer curves from the identical 2D $PtSe_2$ layers after Ar-plasma exposure with varying $V_g$ at 300 K. Unlike the obvious p-type gate response observed in Figure 4b, the Ar-plasma-exposed sample shows significantly suppressed $V_g$ dependency with increased electrical conductance, similar to that in Figure 3e. Upon increasing temperature from 300 to 412 K, the sample also exhibits increased $I_{ds}$, as shown in Figure 4d. However, the degree of this current increase is much smaller than that observed with the initially semiconducting pristine sample (Figure 4b). Plots of temperature-dependent electrical conductance ratio values with respect to that at 300 K, i.e., $S/S_{300}$, are presented for both pristine and Ar-plasma-treated samples in Figure 4e. The pristine sample exhibits a much stronger temperature-dependent conductance increase, reflecting its intrinsic semiconducting nature and thermal generation of charge carriers, consistent with the temperature dependency


https://dx.doi.org/10.1021/acsami.0c00116
ACS Appl. Mater. Interfaces 2020, 12, 14341–14351

observed with 2D $MoS_2$ layers.[55] Moreover, the Ar-plasma-exposed sample exhibits a much weaker temperature dependency of electrical conductance with a smaller increase of $S/S_{300}$, i.e., ∼1.3 compared to ∼2.3 for the pristine sample at 412 K. Although this slight increase of temperature-dependent conductance deviates from the standard behavior of typical metallic materials, this observation is fully consistent with recent studies on the temperature dependency of "metallic" 2D $WSe_2$ layers converted from their initial semiconducting phases.[47] This phenomenon must be attributed to the "incomplete" closing of the band-gap energy of 2D $PtSe_2$ layers and its associated hopping-dominated transports,[47,55] which will be verified in the next section through a DFT calculation study. Moreover, thermal activation energy ($E_a$) values for majority carrier transports were calculated at a given temperature, $T$, using the Arrhenius equation, i.e., $\sigma(T) = \sigma_0 \exp\left(-\frac{E_a}{kT}\right)$, where $\sigma_0$ is the electrical conductivity at $T = 0$ K and $k$ is Boltzmann's constant. Figure 4f displays the Arrhenius plots for both cases, revealing the linear relationship of $\ln \sigma$ vs $\frac{1000}{T}$, where $E_a$ values can be extracted from the slopes of the linear fittings. The activation energies of pristine and Ar-treated 2D $PtSe_2$ layers are 134.43 and 62.04 meV, respectively. The reduced $E_a$ value indicates relaxed band-to-band transports in semiconducting 2D $PtSe_2$ layers after the plasma treatment, further suggesting a reduction of their band-gap energy, to be verified in the next section.

To better clarify the mechanism for the Ar-plasma-induced semiconducting-to-metallic conversion, we performed extensive structural and chemical characterization of 2D $PtSe_2$ layers before/after the Ar-plasma treatment. Figure 5a,b presents the XPS characterization of 2D $PtSe_2$ layers, comparing their core-level spectra of Pt 4f (Figure 5a) and Se 3d (Figure 5b) in pristine vs plasma-treated states. In Figure 5a, the red plot obtained from 2D $PtSe_2$ layers in their pristine state predominantly exhibits the characteristics peaks of $Pt^{4+}$ oxidation states, indicating stoichiometric $PtSe_2$, fully consistent with previous studies.[48] Meanwhile, the blue plot obtained from the identical 2D $PtSe_2$ layers after the Ar-plasma treatment exhibits additional peaks that correspond to $Pt^0$ oxidation states.[56] XPS peak deconvolution analysis identifies the areal ratio of $Pt^{4+}/Pt^0$ to be 53:47, which leads to the Pt/Se atomic ratio of ∼1:1.1. The core-level spectra of Se 3d in Figure 5b also exhibit characteristic peaks corresponding to stoichiometric $PtSe_2$, consistent with previous studies.[48] This XPS analysis suggests that the Ar-plasma treatment leads to the formation of elemental Pt atoms, i.e., increasing amount of $Pt^0$ oxidation states without causing a noticeable change in the oxidation state of Se atoms. The peak intensity decrease observed in Figure 5b indicates a pronounced loss of Se atoms, further to be verified by EDS characterization. Moreover, extensive TEM characterization was performed to unveil a possibility for the formation of any new crystalline phases within 2D $PtSe_2$ layers induced by the Ar plasma. Figure 5c,d presents low-magnification TEM images of 2D $PtSe_2$ layers (left) and their corresponding selected area electron diffraction (SAED) patterns (right) before and after the Ar-plasma treatment, respectively. The TEM and SAED characterization confirms no formation of additional crystalline phases, except for hexagonal $PtSe_2$ crystals. Moreover, the dominant appearance of (110) and (100) SAED ring patterns for both samples indicates that individual 2D $PtSe_2$ layers are horizontally aligned, which is well preserved irrespective of the Ar-plasma treatment, consistent with the previous studies.[26] Figure 5e shows EDS profiles obtained from the 2D $PtSe_2$ layers before/after Ar treatment, corresponding to the TEM images in Figure 5c,d. Pristine 2D $PtSe_2$ layers exhibit a stoichiometric atomic ratio of Pt/Se ∼ 1:2 as anticipated, consistent with the XPS characterization. However, it is interesting to note that the Ar-plasma treatment leads to a Pt-rich compositional change of Pt/Se ∼ 1:$x$, where $x$ = 1.1−1.25, even though there is no signature of new crystalline phase formation or significant structural transformation (SAED in Figure 5d). This combined analysis of XPS, plane-view TEM/SAED, and EDS indicates that 2D $PtSe_2$ layers turn into Pt-rich due to a loss of Se atoms by the Ar-plasma treatment while well retaining their original crystalline integrity. This pronounced loss of Se over Pt caused by external Ar-plasma energy is consistent with the recent observation of significant S loss in 2D $MoS_2$ layers under in situ heating.[57] This phenomenon is attributed to the intrinsically higher volatility of chalcogen components over transition metals, owing to their lower cohesive energies.[58] The chemical conversion takes place according to the following reaction

$$PtSe_2 \rightarrow yPtSe_2 + (1 - y)Pt + (1 - y)\,Se_2 \uparrow$$
$$\text{where } 0.524 \leq y \leq 0.556 \quad (1)$$

Detailed crystalline structures of Ar-plasma-treated 2D $PtSe_2$ layers were characterized by HR-STEM, which was performed for the sample corresponding to the low-magnification TEM in Figure 5d. The HR-STEM image in Figure 5f clarifies the structural distinction of 2D $PtSe_2$ layers after the Ar-plasma treatment, revealing that tiny atomic vacancy-like areas (typically ∼1−3 nm) are "sparsely" observed throughout the entire sample area. The red and blue box regions in Figure 5f are zoomed-in and presented in Figure 5g,h, respectively. Interestingly, we note that Ar-plasma-treated 2D $PtSe_2$ layers still well preserve their high polycrystallinity, as evidenced by the clearly observed crystalline lattice fringes, particularly the Moiré fringe patterns in Figure 5g. We further carried out cross-section TEM characterization of the Ar-plasma-treated 2D $PtSe_2$ layers, and the corresponding cross-sectional TEM image is presented in Figure 5i. We observe that the horizontal alignment of 2D $PtSe_2$ layers is well preserved even after the plasma treatment accompanying the original vdW interlayer spacing of ∼5.3 Å (the inset corresponding to the yellow box) without any discontinuity of individual layers and significant thickness change. We also performed STEM-EDS elemental mapping on the Ar-plasma-treated 2D $PtSe_2$ layers to identify the spatial distribution of constituting Pt and Se atoms. The STEM-EDS elemental map images in Figure 5j reveal a relatively higher intensity of Pt over Se at multiple locations (red and blue circles), which was consistently observed throughout the entire sample area. This very comprehensive structural and chemical analysis suggests that the following events must have occurred by being responsible for the electrically observed semiconducting-to-metallic transition in 2D $PtSe_2$ layers; the mild Ar-plasma treatment employed in this study neither significantly alters the original crystallinity and thickness of 2D $PtSe_2$ layers nor introduces any new crystalline phases. It mainly causes the decomposition of Se atoms, which in turn results in the "spill" of Pt elemental atoms achieving Pt-rich (Se-deficient) $PtSe_x$ layers with $x < 2$. Accordingly, a large concentration of "Se-deficient" atomic


https://dx.doi.org/10.1021/acsami.0c00116
ACS Appl. Mater. Interfaces 2020, 12, 14341−14351

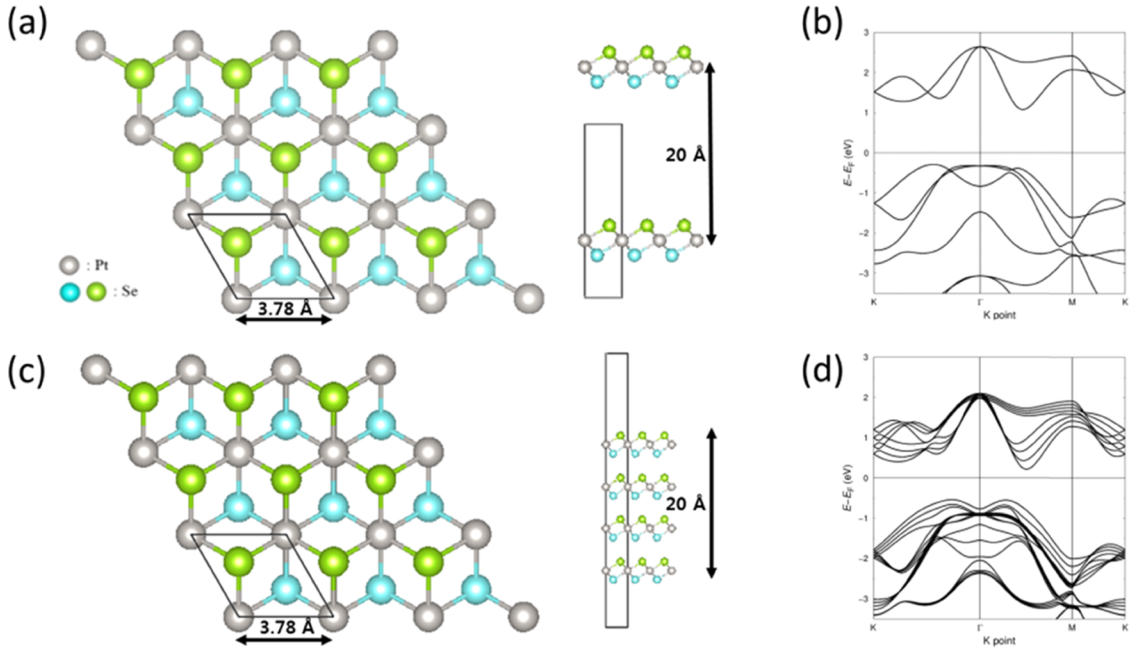


**Figure 6.** DFT calculation of 2D $PtSe_2$ layers in their various pristine forms. Monolayer 2D $PtSe_2$ with its corresponding (a) atomic configuration and (b) band structure. Four-layer 2D $PtSe_2$ with its corresponding (c) atomic configuration and (d) band structure. Both the band structures are presented along K-Γ-M-K points in the hexagonal Brillouin zone.

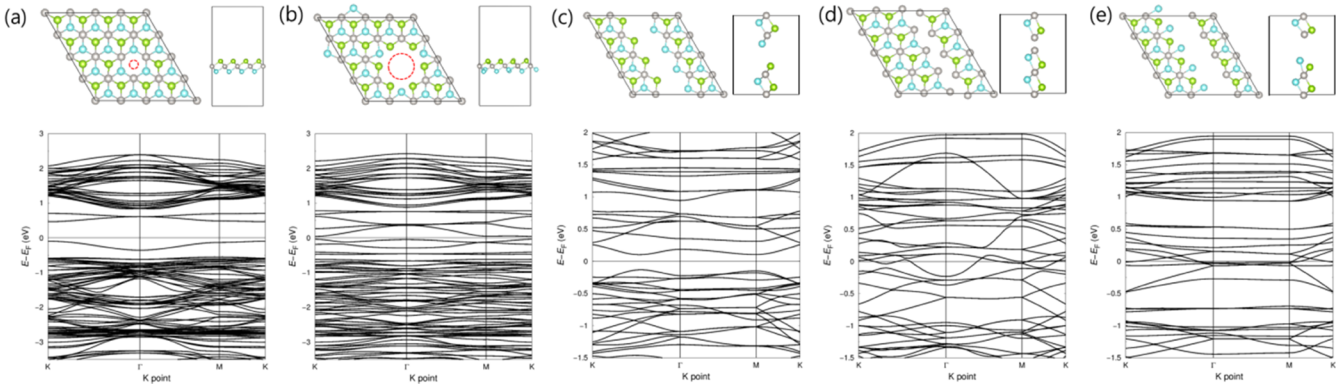


**Figure 7.** DFT calculations of 2D $PtSe_2$ layers containing atomic defects of various forms. Atomic configurations and their corresponding band structures of 2D $PtSe_2$ layers containing single point defects of (a) Se vacancy and (b) nanopores. Atomic configurations and their corresponding band structures of 2D $PtSe_2$ layers containing line defects, which expose (c) Se−Se, (d) Pt−Se, and (e) Pt−Se atoms on the layer edges sites.

vacancies and layer edge sites coupled with exposed Pt nanoparticles formed within 2D basal planes will reduce the original band-gap energy of 2D $PtSe_2$ layers by forming percolated networks for efficient charge carrier transport. In a way to more clearly highlight the structural transition of 2D $PtTe_2$ layers introduced by Ar-plasma treatments, we also compared the TEM images of samples before/after a relatively longer plasma irradiation (>2 min) in the Figure S3, Supporting Information.

To supplement the above experimental analysis and to better clarify the origin of the defect-driven semiconducting-to-metallic conversion, we employed density functional theory (DFT) calculations and investigated the structure−property relationship of 2D $PtSe_2$ layers. We extensively created various defect states in pristine 2D $PtSe_2$ layers and compared their electronic band structures by identifying band-gap energies. We first studied the electronic properties of pristine 2D $PtSe_2$ with varying numbers, i.e., one and four layers, as presented in Figure 6. Figure 6a shows the atomic structure illustration of monolayer 2D $PtSe_2$ in-plane (left) and side (right) views. Figure 6b presents the corresponding electronic band structure, revealing a band-gap energy of ∼1.36 eV. Figure 6c,d presents the atomic structure illustration of four-layer 2D $PtSe_2$ and the corresponding electronic band structure, respectively. With the transition of one-to-four layers, the band-gap energy drastically decreases to ∼0.77 eV, which is qualitatively consistent with previous DFT calculation studies.[53,59] Accordingly, 2D $PtSe_2$ multilayers (four layers, in this case) still retain semiconducting transport properties, which well agrees with our experimental observations (Figures 2e and 3d). For this DFT calculation, the lattice constant of the hexagonal 2D $PtSe_2$ layer is set to be 3.73 Å (Figure 6a,c) and the thickness of each layer is optimized to be 2.58 with ∼20 Å vacuum in between each layer.

We then deliberately created structural defects of various dimensions and types within the basal planes of pristine 2D $PtSe_2$ layers and studied resulting electronic band structures. Figure 7a presents the case of a single Se atomic vacancy



https://dx.doi.org/10.1021/acsami.0c00116
ACS Appl. Mater. Interfaces 2020, 12, 14341−14351

Table 1. Overview of the Recently Developed FET Devices Based on 2D $PtSe_2$ Layers

| preparation method | device fabrication | layer number/thickness (nm) | device area | channel dimension | gate configuration | carrier type | ref |
|---|---|---|---|---|---|---|---|
| CVD and mechanical exfoliation | e-beam lithography | 8 | micrometer scale | micrometer scale | back gated | n-type | 15 |
| mechanical exfoliation from commercial crystals | e-beam lithography | 2 | micrometer scale | micrometer scale | back gated | n-type | 51 |
| | | 5 | micrometer scale | micrometer scale | back gated | n-type | |
| CVD and transfer to secondary substrates | photolithography | 2.5−3 | centimeter scale | centimeter scale | back gated | p-type | 53 |
| | | 5−6.5 | centimeter scale | micrometer scale | back gated | p-type | |
| CVD | photolithography | 4 | NA | micrometer scale | buried | p-type | 64 |
| | | 8 | | | | | |
| | | 12 | | | | | |
| plasma-assisted selenization | photolithography | 2.5 | NA | micrometer scale | back gated | P type | 26 |
| | | 3.5 | | | | | |
| CVD | e-beam lithography | 3−10 | nanometer scale | nanometer scale | back gated | P type | 65 |
| mechanical exfoliation from commercial crystals | e-beam lithography | 3 | micrometer scale | micrometer scale | back gated | P type | 66 |
| CVD | e-beam lithography | 2−2.5 nm | NA | micrometer scale | | P type | 17 |
| CVD and transfer to secondary substrates | shadow mask | ∼3 nm | centimeter scale | micrometer scale | back gated | P type | this work |

present on the basal plane, whose atomic configuration is illustrated in the top panel image. The bottom panel image shows the corresponding electronic band structure, revealing the band-gap energy of 0.56 eV, which is significantly smaller than that of the 2D $PtSe_2$ layer without the defect shown in Figure 6a. Figure 7b presents a 2D $PtSe_2$ layer containing a large pore missing three Pt atoms and four Se atoms within its basal plane, as illustrated in the top panel image. The corresponding electronic band structure presented in the bottom panel image exhibits that its band-gap energy is 0.07 eV, indicating that it is nearly metallic with an increasing number of defects. The area densities of the Se vacancy (Figure 7a) and the nanopore (Figure 7b) are set to be $5.2 \times 10^{-3}$ atom/Å$^2$ and $5.2 \times 10^{-3}$ pore/Å$^2$, respectively. Figure 7c−e presents the cases of line defects within the basal plane of a 2D $PtSe_2$ layer, exposing three different types of atomic defects on the 2D edge site, i.e., Se−Se, Pt−Pt, and Pt−Se atoms, respectively. While the Se−Se-exposed Pt-deficient 2D layer exhibits a small band-gap energy of 0.24 eV (Figure 7c), the 2D layers exposing Pt−Pt atoms (thus Se-deficient) and Pt−Se atoms are nearly metallic (Figure 7d−e). This DFT calculation indicates that semiconducting pristine 2D $PtSe_2$ layers can be externally converted into metallic with an increasing concentration of atomic defects toward Se-deficient states, which is fully consistent with our FET and TEM observations. Finally, we overview the geometrical and operational parameters as well as preparation methods for recently developed FET devices based on semiconducting 2D $PtSe_2$ layers, as presented in Table 1.

## CONCLUSIONS

We irradiated wafer-scale CVD-grown few-layer 2D $PtSe_2$ samples with controlled Ar plasma and externally converted their intrinsic semiconducting properties into metallic transports, confirmed by FET measurements. By employing extensive structural and chemical characterization, we identified that the plasma-irradiated initially stoichiometric 2D $PtSe_2$ layers became Se-deficient while well preserving their overall crystallinity. Furthermore, we performed DFT calculations and clarified that Se-deficient defective 2D $PtSe_2$ layers gradually close their band-gap energy with an increasing number of atomic defects, introducing various midgap energy states. This corroborative experimental and theoretical study fully accounts for the origin of the externally modulated semiconducting-to-metallic conversion in 2D $PtSe_2$ layers, suggesting their extended technological implications for near-atom-thickness electronic devices.

## EXPERIMENTAL SECTION

**Material Synthesis.** Wafer-scale 2D $PtSe_2$ layers were grown by the CVD conversion of Pt thin films at 400 °C, as reported previously.[48] Pt thin films of controlled thickness were deposited on $SiO_2$/Si wafers by an electron beam evaporator (Thermionics VE-100) at a fixed evaporation rate of 0.15 Å/s. Pt-deposited substrates were placed in the center zone of a home-built CVD chamber (Lindberg/Blue M Mini-Mite) with an alumina boat containing Se powder preloaded at the upstream side. The CVD chamber was then evacuated to a base pressure of ∼1 mTorr and purged with Ar gas several times. Subsequently, it was heated to the growth temperature of 400 °C, which was retained for 50 min under a constant flow of Ar gas at ∼100 standard cubic centimeters per minute (SCCM).

**Ar-Plasma Treatment.** Two-dimensional (2D) $PtSe_2$ layers prepared by the TRT method described in the main text were placed inside the Ar-plasma chamber (Harrick Plasma, model PDC-32G). Following initial evacuation down to ∼10−25 mTorr, Ar gas of 10 psi pressure was flown into the chamber at a rate of 20 mL/min, achieving a chamber pressure of 204 mTorr using a gas flow controller (PlasmaFlo PDC-FMG). Then, plasma was activated, and its power was maintained at 11 W for controlled duration times (typically from 30 s to ∼2−3 min).

**Raman Characterization.** Raman characterization was performed using an inVia confocal Raman microscope system (Renishaw) in ambient conditions at room temperature. A laser source of 523 nm wavelength was used, and the excitation power was set to be 1 mW.

**TEM/STEM Characterization.** Structural and chemical analyses of 2D $PtSe_2$ layers were performed using FEI F30 Cs-corrected TEM. For plane-view TEM imaging, as-prepared 2D $PtSe_2$ layers were transferred to copper TEM grids by the previously reported wet


https://dx.doi.org/10.1021/acsami.0c00116
ACS Appl. Mater. Interfaces 2020, 12, 14341−14351

etching method.[48] Cross-sectional TEM samples were prepared by focused ion beam (FIB) TEM lift-out techniques.

**FET Fabrication and Characterization.** As-prepared 2D $PtSe_2$ layers were manually integrated on $SiO_2$/Si wafers ($SiO_2$ thickness: 300 nm) by the TRT method described in the main text. Subsequently, Au top electrodes (60 nm) were deposited by DC sputtering through a shadow mask, defining the channel length to be 50 $\mu$m. All electrical measurements were performed with a home-built probe station using an HP 4156 A semiconductor parameter analyzer.

**Variant-Temperature Electrical Measurements.** For temperature-variant electrical measurements, devices were probed under vacuum inside a Janis research ST-500-UHT micromanipulated probe station, and the temperature was varied with a Lakeshore 336 cryogenic temperature controller. Electrical measurements were carried out with a Keysight B1500A semiconductor device analyzer.

**DFT Calculations.** DFT calculations were performed using the Vienna ab initio simulation package (VASP), and the wave functions were approximated with the projector-augmented wave (PAW) pseudopotentials.[60,61] The exchange-correlation functional was described by the generalized gradient approximation (GGA) of Perdew–Burke–Ernzerhof (PBE) parameters.[62,63] A cutoff energy of 500 eV was used, and geometry optimization was performed until the energy convergence satisfied the criterion of $1.0 \times 10^{-7}$ eV/Å. The atomic positions of 2D $PtSe_2$ layers were relaxed from the optimized geometry. The first Brillouin zone was sampled with the Monkhorst–Pack grid of $6 \times 6 \times 1$ $k$ points for four-layer 2D $PtSe_2$ and $3 \times 3 \times 1$ $k$ points for pristine and defect-containing monolayer 2D $PtSe_2$.

## ■ ASSOCIATED CONTENT

### Supporting Information

The Supporting Information is available free of charge at https://pubs.acs.org/doi/10.1021/acsami.0c00116.

> Representative characteristics of $I_{ds}$ vs $V_{ds}$ with varying $V_g$ obtained from an unoptimized FET device directly irradiated with Ar plasma after its fabrication; AFM image and height profile for a sample in its pristine state and after a mild Ar plasma treatment; HRTEM images of 2D $PtSe_2$ layers obtained before and after a prolonged Ar plasma treatment (PDF)

## ■ AUTHOR INFORMATION


### Corresponding Authors

**YounJoon Jung** − *Department of Chemistry, Seoul National University, Seoul 08826, South Korea;* orcid.org/0000-0002-9464-9999; Email: yjjung@snu.ac.kr

**Yeonwoong Jung** − *NanoScience Technology Center, Department of Electrical and Computer Engineering, and Department of Materials Science and Engineering, University of Central Florida, Orlando, Florida 32826, United States;* orcid.org/0000-0001-6042-5551; Email: Yeonwoong.Jung@ucf.edu

### Authors

**Mashiyat Sumaiya Shawkat** − *NanoScience Technology Center and Department of Electrical and Computer Engineering, University of Central Florida, Orlando, Florida 32826, United States;* orcid.org/0000-0001-6594-190X

**Jaeyoung Gil** − *Department of Chemistry, Seoul National University, Seoul 08826, South Korea*

**Sang Sub Han** − *NanoScience Technology Center, University of Central Florida, Orlando, Florida 32826, United States; Department of Materials Science and Engineering, Seoul National University, Seoul 08826, South Korea*

**Tae-Jun Ko** − *NanoScience Technology Center, University of Central Florida, Orlando, Florida 32826, United States*

**Mengjing Wang** − *NanoScience Technology Center, University of Central Florida, Orlando, Florida 32826, United States;* orcid.org/0000-0003-1195-4515

**Durjoy Dev** − *NanoScience Technology Center and Department of Electrical and Computer Engineering, University of Central Florida, Orlando, Florida 32826, United States*

**Junyoung Kwon** − *Department of Materials Science and Engineering, Yonsei University, Seoul 03722, South Korea*

**Gwan-Hyoung Lee** − *Department of Materials Science and Engineering, Seoul National University, Seoul 08826, South Korea;* orcid.org/0000-0002-3028-867X

**Kyu Hwan Oh** − *Department of Materials Science and Engineering, Seoul National University, Seoul 08826, South Korea*

**Hee-Suk Chung** − *Analytical Research Division, Korea Basic Science Institute, Jeonju 54907, South Korea*

**Tania Roy** − *NanoScience Technology Center, Department of Electrical and Computer Engineering, and Department of Materials Science and Engineering, University of Central Florida, Orlando, Florida 32826, United States;* orcid.org/0000-0003-1131-8068

Complete contact information is available at: https://pubs.acs.org/10.1021/acsami.0c00116


### Author Contributions

△M.S.S. and J.G. equally contributed to the work. Y.J. (UCF) conceived the project and directed it. M.S.S. prepared 2D $PtSe_2$ layers and performed the Ar-plasma treatment with the assistance of T.-J.K. M.S.S. fabricated the FET devices and performed their measurements with the assistance of S.S.H. H.-S.C. performed the TEM/STEM characterization and analyzed the data. S.S.H. and M.W. assisted the analysis of TEM/STEM data under the guidance of K.H.O. D.D. and M.S.S. performed the variant-temperature electrical measurement under the guidance of T.R. J.K. assisted the FET measurement and Raman characterization under the guidance of G.-H.L. M.S.S. performed the XPS characterization under the guidance of Y.J. (UCF). J.G. performed the DFT calculation and analyzed the data under the guidance of Y.J. (SNU). M.S.S., J.G., Y.J., and Y.J. wrote the manuscript with inputs from all authors.

### Notes

The authors declare no competing financial interest.

## ■ ACKNOWLEDGMENTS

Y.J. acknowledges financial support from the National Science Foundation (CMMI-1728390) (M.S.S. and Y.J.), the Korea Institute of Energy Technology Evaluation and Planning (KETEP) and the Ministry of Trade, Industry & Energy (MOTIE) of the Republic of Korea (No. 20173010013340), and the VPR Advancement of Early Career Researchers award from the University of Central Florida. This research was in part supported by the Creative Materials Discovery Program through the National Research Foundation of Korea (NRF) funded by the Ministry of Science, ICT and Future Planning (NRF-2017M3D1A1039553). The work at SNU was supported by the National Research Foundation of Korea (NRF-2018R1D1A1B07043973, 2017R1A5A1014862, SRC program: vdWMRC center) and Creative-Pioneering Researchers Program through Seoul National University (SNU). H.S.C. was supported by the National Research Foundation of Korea (NRF) grant funded by the Korea government (MSIT) (No. 2019R1F1A1058410).



https://dx.doi.org/10.1021/acsami.0c00116
ACS Appl. Mater. Interfaces 2020, 12, 14341−14351

## REFERENCES


(1) Manzeli, S.; Ovchinnikov, D.; Pasquier, D.; Yazyev, O. V.; Kis, A. 2D Transition Metal Dichalcogenides. *Nat. Rev. Mater.* **2017**, *2*, No. 17033.

(2) Chhowalla, M.; Shin, H. S.; Eda, G.; Li, L.-J.; Loh, K. P.; Zhang, H. The Chemistry of Two-Dimensional Layered Transition Metal Dichalcogenide Nanosheets. *Nat. Chem.* **2013**, *5*, 263−275.

(3) Mak, K. F.; Shan, J. Photonics and Optoelectronics of 2D Semiconductor Transition Metal Dichalcogenides. *Nat. Photonics* **2016**, *10*, 216−226.

(4) Akinwande, D.; Petrone, N.; Hone, J. Two-Dimensional Flexible Nanoelectronics. *Nat. Commun.* **2014**, *5*, No. 5678.

(5) Chia, X.; Eng, A. Y. S.; Ambrosi, A.; Tan, S. M.; Pumera, M. Electrochemistry of Nanostructured Layered Transition-Metal Dichalcogenides. *Chem. Rev.* **2015**, *115*, 11941−11966.

(6) Choudhary, N.; Islam, M. A.; Kim, J. H.; Ko, T.-J.; Schropp, A.; Hurtado, L.; Weitzman, D.; Zhai, L.; Jung, Y. Two-Dimensional Transition Metal Dichalcogenide Hybrid Materials for Energy Applications. *Nano Today* **2018**, *19*, 16−40.

(7) Jariwala, D.; Sangwan, V. K.; Lauhon, L. J.; Marks, T. J.; Hersam, M. C. Emerging Device Applications for Semiconducting Two-Dimensional Transition Metal Dichalcogenides. *ACS Nano* **2014**, *8*, 1102−1120.

(8) Bhimanapati, G. R.; Lin, Z.; Meunier, V.; Jung, Y.; Cha, J.; Das, S.; Xiao, D.; Son, Y.; Strano, M. S.; Cooper, V. R.; Liang, L.; Louie, S. G.; Ringe, E.; Zhou, W.; Kim, S. S.; Naik, R. R.; Sumpter, B. G.; Terrones, H.; Xia, F.; Wang, Y.; Zhu, J.; Akinwande, D.; Alem, N.; Schuller, J. A.; Schaak, R. E.; Terrones, M.; Robinson, J. A. Recent Advances in Two-Dimensional Materials Beyond Graphene. *ACS Nano* **2015**, *9*, 11509−11539.

(9) Gupta, A.; Sakthivel, T.; Seal, S. Recent Development in 2D Materials Beyond Graphene. *Prog. Mater. Sci.* **2015**, *73*, 44−126.

(10) Jiang, S.; Zhang, Z.; Zhang, N.; Huan, Y.; Gong, Y.; Sun, M.; Shi, J.; Xie, C.; Yang, P.; Fang, Q.; Li, H.; Tong, L.; Xie, D.; Gu, L.; Liu, P.; Zhang, Y. Application of Chemical Vapor−Deposited Monolayer $ReSe_2$ in the Electrocatalytic Hydrogen Evolution Reaction. *Nano Res.* **2018**, *11*, 1787−1797.

(11) Jiang, S.; Hong, M.; Wei, W.; Zhao, L.; Zhang, N.; Zhang, Z.; Yang, P.; Gao, N.; Zhou, X.; Xie, C.; Shi, J.; Huan, Y.; Tong, L.; Zhao, J.; Zhang, Q.; Fu, Q.; Zhang, Y. Direct Synthesis and In Situ Characterization of Monolayer Parallelogrammic Rhenium Diselenide on Gold Foil. *Commun. Chem.* **2018**, *1*, No. 17.

(12) Pi, L.; Li, L.; Liu, K.; Zhang, Q.; Li, H.; Zhai, T. Recent Progress on 2D Noble-Transition-Metal Dichalcogenides. *Adv. Funct. Mater.* **2019**, *29*, No. 1904932.

(13) Jiang, S.; Xie, C.; Gu, Y.; Zhang, Q.; Wu, X.; Sun, Y.; Li, W.; Shi, Y.; Zhao, L.; Pan, S.; Yang, P.; Huan, Y.; Xie, D.; Zhang, Q.; Liu, X.; Zou, X.; Gu, L.; Zhang, Y. Anisotropic Growth and Scanning Tunneling Microscopy Identification of Ultrathin Even-Layered $PdSe_2$ Ribbons. *Small* **2019**, *15*, No. 1902789.

(14) Zhang, W.; Huang, Z.; Zhang, W.; Li, Y. Two-Dimensional Semiconductors with Possible High Room Temperature Mobility. *Nano Res.* **2014**, *7*, 1731−1737.

(15) Zhao, Y.; Qiao, J.; Yu, Z.; Yu, P.; Xu, K.; Lau, S. P.; Zhou, W.; Liu, Z.; Wang, X.; Ji, W.; Chai, Y. High-Electron-Mobility and Air-Stable 2D Layered $PtSe_2$ FETs. *Adv. Mater.* **2017**, *29*, No. 1604230.

(16) Radisavljevic, B.; Radenovic, A.; Brivio, J.; Giacometti, V.; Kis, A. Single-Layer $MoS_2$ Transistors. *Nat. Nanotechnol.* **2011**, *6*, 147−150.

(17) Yim, C.; Passi, V.; Lemme, M. C.; Duesberg, G. S.; Coileáin, C. Ó.; Pallecchi, E.; Fadil, D.; McEvoy, N. Electrical Devices from Top-Down Structured Platinum Diselenide Films. *npj 2D Mater. Appl.* **2018**, *2*, No. 5.

(18) Yim, C.; Lee, K.; McEvoy, N.; O'Brien, M.; Riazimehr, S.; Berner, N. C.; Cullen, C. P.; Kotakoski, J.; Meyer, J. C.; Lemme, M. C.; Duesberg, G. S. High-Performance Hybrid Electronic Devices from Layered $PtSe_2$ Films Grown at Low Temperature. *ACS Nano* **2016**, *10*, 9550−9558.

(19) Jung, Y.; Shen, J.; Liu, Y.; Woods, J. M.; Sun, Y.; Cha, J. J. Metal Seed Layer Thickness-Induced Transition from Vertical to Horizontal Growth of $MoS_2$ and $WS_2$. *Nano Lett.* **2014**, *14*, 6842−6849.

(20) Islam, M. A.; Church, J.; Han, C.; Chung, H.-S.; Ji, E.; Kim, J. H.; Choudhary, N.; Lee, G.-H.; Lee, W. H.; Jung, Y. Noble Metal-Coated $MoS_2$ Nanofilms with Vertically-Aligned 2D Layers for Visible Light-Driven Photocatalytic Degradation of Emerging Water Contaminants. *Sci. Rep.* **2017**, *7*, No. 14944.

(21) Okogbue, E.; Han, S. S.; Ko, T.-J.; Chung, H.-S.; Ma, J.; Shawkat, M. S.; Kim, J. H.; Kim, J. H.; Ji, E.; Oh, K. H.; Zhai, L.; Lee, G.-H.; Jung, Y. Multifunctional Two-Dimensional $PtSe_2$-Layer Kirigami Conductors with 2000% Stretchability and Metallic-to-Semiconducting Tunability. *Nano Lett.* **2019**, *19*, 7598−7607.

(22) Yu, X.; Yu, P.; Wu, D.; Singh, B.; Zeng, Q.; Lin, H.; Zhou, W.; Lin, J.; Suenaga, K.; Liu, Z.; Wang, Q. J. Atomically Thin Noble Metal Dichalcogenide: A Broadband Mid-Infrared Semiconductor. *Nat. Commun.* **2018**, *9*, No. 1545.

(23) Shi, J.; Huan, Y.; Hong, M.; Xu, R.; Yang, P.; Zhang, Z.; Zou, X.; Zhang, Y. Chemical Vapor Deposition Grown Large-Scale Atomically Thin Platinum Diselenide with Semimetal−Semiconductor Transition. *ACS Nano* **2019**, *13*, 8442−8451.

(24) Absor, M. A. U.; Santoso, I.; Harsojo; Abraha, K.; Ishii, F.; Saito, M. Defect-Induced Large Spin-Orbit Splitting in Monolayer PtSe2. *Phys. Rev. B* **2017**, *96*, No. 115128.

(25) Avsar, A.; Ciarrocchi, A.; Pizzochero, M.; Unuchek, D.; Yazyev, O. V.; Kis, A. Defect Induced, Layer-Modulated Magnetism in Ultrathin Metallic $PtSe_2$. *Nat. Nanotechnol.* **2019**, *14*, 674−678.

(26) Su, T.-Y.; Medina, H.; Chen, Y.-Z.; Wang, S.-W.; Lee, S.-S.; Shih, Y.-C.; Chen, C.-W.; Kuo, H.-C.; Chuang, F.-C.; Chueh, Y.-L. Phase-Engineered $PtSe_2$-Layered Films by a Plasma-Assisted Selenization Process toward All $PtSe_2$-Based Field Effect Transistor to Highly Sensitive, Flexible, and Wide-Spectrum Photoresponse Photodetectors. *Small* **2018**, *14*, No. 1800032.

(27) Ling, X.; Lin, Y.; Ma, Q.; Wang, Z.; Song, Y.; Yu, L.; Huang, S.; Fang, W.; Zhang, X.; Hsu, A. L.; Bie, Y.; Lee, Y.-H.; Zhu, Y.; Wu, L.; Li, J.; Jarillo-Herrero, P.; Dresselhaus, M.; Palacios, T.; Kong, J. Parallel Stitching of 2D Materials. *Adv. Mater.* **2016**, *28*, 2322−2329.

(28) Zhao, M.; Ye, Y.; Han, Y.; Xia, Y.; Zhu, H.; Wang, S.; Wang, Y.; Muller, D. A.; Zhang, X. Large-Scale Chemical Assembly of Atomically Thin Transistors and Circuits. *Nat. Nanotechnol.* **2016**, *11*, 954−959.

(29) Wagner, S.; Yim, C.; McEvoy, N.; Kataria, S.; Yokaribas, V.; Kuc, A.; Pindl, S.; Fritzen, C.-P.; Heine, T.; Duesberg, G. S.; Lemme, M. C. Highly Sensitive Electromechanical Piezoresistive Pressure Sensors Based on Large-Area Layered $PtSe_2$ Films. *Nano Lett.* **2018**, *18*, 3738−3745.

(30) Boland, C. S.; Coileáin, C. Ó.; Wagner, S.; McManus, J. B.; Cullen, C. P.; Lemme, M. C.; Duesberg, G. S.; McEvoy, N. $PtSe_2$ Grown Directly on Polymer Foil for Use as a Robust Piezoresistive Sensor. *2D Mater.* **2019**, *6*, No. 045029.

(31) Sajjad, M.; Montes, E.; Singh, N.; Schwingenschlögl, U. Superior Gas Sensing Properties of Monolayer $PtSe_2$. *Adv. Mater. Interfaces* **2017**, *4*, No. 1600911.

(32) Guo, S.-D. Biaxial Strain Tuned Thermoelectric Properties in Monolayer $PtSe_2$. *J. Mater. Chem. C* **2016**, *4*, 9366−9374.

(33) Moon, H.; Bang, J.; Hong, S.; Kim, G.; Roh, J. W.; Kim, J.; Lee, W. Strong Thermopower Enhancement and Tunable Power Factor via Semimetal to Semiconductor Transition in a Transition-Metal Dichalcogenide. *ACS Nano* **2019**, *13*, 13317−13324.

(34) Wu, D.; Wang, Y.; Zeng, L.; Jia, C.; Wu, E.; Xu, T.; Shi, Z.; Tian, Y.; Li, X.; Tsang, Y. H. Design of 2D Layered $PtSe_2$ Heterojunction for the High-Performance, Room-Temperature, Broadband, Infrared Photodetector. *ACS Photonics* **2018**, *5*, 3820−3827.

(35) Yim, C.; McEvoy, N.; Riazimehr, S.; Schneider, D. S.; Gity, F.; Monaghan, S.; Hurley, P. K.; Lemme, M. C.; Duesberg, G. S. Wide Spectral Photoresponse of Layered Platinum Diselenide-Based Photodiodes. *Nano Lett.* **2018**, *18*, 1794−1800.




https://dx.doi.org/10.1021/acsami.0c00116
*ACS Appl. Mater. Interfaces* 2020, 12, 14341−14351

(36) Shawkat, M. S.; Chung, H.-S.; Dev, D.; Das, S.; Roy, T.; Jung, Y. Two-Dimensional/Three-Dimensional Schottky Junction Photovoltaic Devices Realized by the Direct CVD Growth of vdW 2D $PtSe_2$ Layers on Silicon. *ACS Appl. Mater. Interfaces* **2019**, *11*, 27251−27258.
(37) Xie, C.; Zeng, L.; Zhang, Z.; Tsang, Y.-H.; Luo, L.; Lee, J.-H. High-Performance Broadband Heterojunction Photodetectors Based on Multilayered $PtSe_2$ Directly Grown on a Si Substrate. *Nanoscale* **2018**, *10*, 15285−15293.
(38) Zeng, L.; Lin, S.; Lou, Z.; Yuan, H.; Long, H.; Li, Y.; Lu, W.; Lau, S. P.; Wu, D.; Tsang, Y. H. Ultrafast and Sensitive Photodetector Based on a $PtSe_2$/Silicon Nanowire Array Heterojunction with a Multiband Spectral Response from 200 to 1550 nm. *NPG Asia Mater.* **2018**, *10*, 352−362.
(39) Zeng, L.-H.; Lin, S.-H.; Li, Z.-J.; Zhang, Z.-X.; Zhang, T.-F.; Xie, C.; Mak, C.-H.; Chai, Y.; Lau, S. P.; Luo, L.-B.; Tsang, Y. H. Fast, Self-Driven, Air-Stable, and Broadband Photodetector Based on Vertically Aligned $PtSe_2$/GaAs Heterojunction. *Adv. Funct. Mater.* **2018**, *28*, No. 1705970.
(40) Zhang, Z.-X.; Long-Hui, Z.; Tong, X.-W.; Gao, Y.; Xie, C.; Tsang, Y. H.; Luo, L.-B.; Wu, Y.-C. Ultrafast, Self-Driven, and Air-Stable Photodetectors Based on Multilayer $PtSe_2$/Perovskite Heterojunctions. *J. Phys. Chem. Lett.* **2018**, *9*, 1185−1194.
(41) Zhuo, R.; Zeng, L.; Yuan, H.; Wu, D.; Wang, Y.; Shi, Z.; Xu, T.; Tian, Y.; Li, X.; Tsang, Y. H. In-Situ Fabrication of $PtSe_2$/GaN Heterojunction for Self-Powered Deep Ultraviolet Photodetector with Ultrahigh Current On/Off Ratio and Detectivity. *Nano Res.* **2019**, *12*, 183−189.
(42) Wang, L.; Li, J.-J.; Fan, Q.; Huang, Z.-F.; Lu, Y.-C.; Xie, C.; Wu, C.-Y.; Luo, L.-B. A High-Performance Near-Infrared Light Photovoltaic Detector Based on a Multilayered $PtSe_2$/Ge Heterojunction. *J. Mater. Chem. C* **2019**, *7*, 5019−5027.
(43) Cho, S.; Kim, S.; Kim, J. H.; Zhao, J.; Seok, J.; Keum, D. H.; Baik, J.; Choe, D.-H.; Chang, K. J.; Suenaga, K.; Kim, S. W.; Lee, Y. H.; Yang, H. Phase Patterning for Ohmic Homojunction Contact in $MoTe_2$. *Science* **2015**, *349*, 625−628.
(44) Fox, D. S.; Zhou, Y.; Maguire, P.; O'Neill, A.; Ó'Coileáin, C.; Gatensby, R.; Glushenkov, A. M.; Tao, T.; Duesberg, G. S.; Shvets, I. V.; Abid, M.; Abid, M.; Wu, H.-C.; Chen, Y.; Coleman, J. N.; Donegan, J. F.; Zhang, H. Nanopatterning and Electrical Tuning of $MoS_2$ Layers with a Subnanometer Helium Ion Beam. *Nano Lett.* **2015**, *15*, 5307−5313.
(45) Stanford, M. G.; Pudasaini, P. R.; Belianinov, A.; Cross, N.; Noh, J. H.; Koehler, M. R.; Mandrus, D. G.; Duscher, G.; Rondinone, A. J.; Ivanov, I. N.; Ward, T. Z.; Rack, P. D. Focused Helium-Ion Beam Irradiation Effects on Electrical Transport Properties of Few-Layer $WSe_2$: Enabling Nanoscale Direct Write Homo-Junctions. *Sci. Rep.* **2016**, *6*, No. 27276.
(46) Qiu, H.; Xu, T.; Wang, Z.; Ren, W.; Nan, H.; Ni, Z.; Chen, Q.; Yuan, S.; Miao, F.; Song, F.; Long, G.; Shi, Y.; Sun, L.; Wang, J.; Wang, X. Hopping Transport Through Defect-Induced Localized States in Molybdenum Disulphide. *Nat. Commun.* **2013**, *4*, No. 2642.
(47) Stanford, M. G.; Pudasaini, P. R.; Gallmeier, E. T.; Cross, N.; Liang, L.; Oyedele, A.; Duscher, G.; Mahjouri-Samani, M.; Wang, K.; Xiao, K.; Geohegan, D. B.; Belianinov, A.; Sumpter, B. G.; Rack, P. D. High Conduction Hopping Behavior Induced in Transition Metal Dichalcogenides by Percolating Defect Networks: Toward Atomically Thin Circuits. *Adv. Funct. Mater.* **2017**, *27*, No. 1702829.
(48) Han, S. S.; Kim, J. H.; Noh, C.; Kim, J. H.; Ji, E.; Kwon, J.; Yu, S. M.; Ko, T.-J.; Okogbue, E.; Oh, K. H.; Chung, H.-S.; Jung, Y.; Lee, G.-H.; Jung, Y. Horizontal-to-Vertical Transition of 2D Layer Orientation in Low-Temperature Chemical Vapor Deposition-Grown $PtSe_2$ and Its Influences on Electrical Properties and Device Applications. *ACS Appl. Mater. Interfaces* **2019**, *11*, 13598−13607.
(49) Kim, J. H.; Ko, T.-J.; Okogbue, E.; Han, S. S.; Shawkat, M. S.; Kaium, M. G.; Oh, K. H.; Chung, H.-S.; Jung, Y. Centimeter-Scale Green Integration of Layer-by-Layer 2D TMD vdW Heterostructures on Arbitrary Substrates by Water-Assisted Layer Transfer. *Sci. Rep.* **2019**, *9*, No. 1641.
(50) Hu, D.; Zhao, T.; Ping, X.; Zheng, H.; Xing, L.; Liu, X.; Zheng, J.; Sun, L.; Gu, L.; Tao, C.; Wang, D.; Jiao, L. Unveiling the Layer-Dependent Catalytic Activity of $PtSe_2$ Atomic Crystals for the Hydrogen Evolution Reaction. *Angew. Chem.* **2019**, *131*, 7051−7055.
(51) Ciarrocchi, A.; Avsar, A.; Ovchinnikov, D.; Kis, A. Thickness-Modulated Metal-to-Semiconductor Transformation in a Transition Metal Dichalcogenide. *Nat. Commun.* **2018**, *9*, No. 919.
(52) Wang, L.; Zhang, S.; McEvoy, N.; Sun, Y.-y.; Huang, J.; Xie, Y.; Dong, N.; Zhang, X.; Kislyakov, I. M.; Nunzi, J.-M.; Zhang, L.; Wang, J. Nonlinear Optical Signatures of the Transition from Semiconductor to Semimetal in $PtSe_2$. *Laser Photonics Rev.* **2019**, *13*, No. 1900052.
(53) Ansari, L.; Monaghan, S.; McEvoy, N.; Coileáin, C. Ó.; Cullen, C. P.; Lin, J.; Siris, R.; Stimpel-Lindner, T.; Burke, K. F.; Mirabelli, G.; Duffy, R.; Caruso, E.; Nagle, R. E.; Duesberg, G. S.; Hurley, P. K.; Gity, F. Quantum Confinement-Induced Semimetal-to-Semiconductor Evolution in Large-Area Ultra-Thin $PtSe_2$ Films Grown at 400 °C. *npj 2D Mater. Appl.* **2019**, *3*, No. 33.
(54) Huang, B.; Tian, F.; Shen, Y.; Zheng, M.; Zhao, Y.; Wu, J.; Liu, Y.; Pennycook, S. J.; Thong, J. T. L. Selective Engineering of Chalcogen Defects in $MoS_2$ by Low-Energy Helium Plasma. *ACS Appl. Mater. Interfaces* **2019**, *11*, 24404−24411.
(55) Nayak, A. P.; Bhattacharyya, S.; Zhu, J.; Liu, J.; Wu, X.; Pandey, T.; Jin, C.; Singh, A. K.; Akinwande, D.; Lin, J.-F. Pressure-Induced Semiconducting to Metallic Transition in Multilayered Molybdenum Disulphide. *Nat. Commun.* **2014**, *5*, No. 3731.
(56) Dückers, K.; Bonzel, H. P.; Wesner, D. A. Surface Core Level Shifts of Pt(111) Measured with Y M$\chi$ Radiation (132.3 eV). *Surf. Sci.* **1986**, *166*, 141−158.
(57) Wang, M.; Kim, J. H.; Han, S. S.; Je, M.; Gil, J.; Noh, C.; Ko, T.-J.; Lee, K. S.; Son, D. I.; Bae, T.-S.; Ryu, H. I.; Oh, K. H.; Jung, Y.; Choi, H.; Chung, H.-S.; Jung, Y. Structural Evolutions of Vertically Aligned Two-Dimensional $MoS_2$ Layers Revealed by in Situ Heating Transmission Electron Microscopy. *J. Phys. Chem. C* **2019**, *123*, 27843−27853.
(58) Kittel, C. *Introduction to Solid State Physics*, 8ed.; John Wiley & Sons, Inc.: Hoboken, NJ, 2005.
(59) Villaos, R. A. B.; Crisostomo, C. P.; Huang, Z.-Q.; Huang, S.-M.; Padama, A. A. B.; Albao, M. A.; Lin, H.; Chuang, F.-C. Thickness Dependent Electronic Properties of Pt Dichalcogenides. *npj 2D Mater. Appl.* **2019**, *3*, No. 2.
(60) Kresse, G.; Furthmüller, J. Efficient Iterative Schemes for Ab Initio Total-Energy Calculations Using a Plane-Wave Basis Set. *Phys. Rev. B* **1996**, *54*, 11169.
(61) Kresse, G.; Joubert, D. From Ultrasoft Pseudopotentials to the Projector Augmented-Wave Method. *Phys. Rev. B* **1999**, *59*, 1758.
(62) Perdew, J. P.; Burke, K.; Ernzerhof, M. Generalized Gradient Approximation Made Simple. *Phys. Rev. Lett.* **1996**, *77*, 3865.
(63) Perdew, J. P.; Burke, K.; Ernzerhof, M. Erratum: Generalized Gradient Approximation Made Simple. *Phys. Rev. Lett.* **1997**, *78*, No. 1396.
(64) Li, L.; Xiong, K.; Marsell, R. J.; Madjar, A.; Strandwitz, N. C.; Hwang, J. C. M.; McEvoy, N.; McManus, J. B.; Duesberg, G. S.; Göritz, A.; Wietstruck, M.; Kaynak, M. Wafer-Scale Fabrication of Recessed-Channel $PtSe_2$ MOSFETs With Low Contact Resistance and Improved Gate Control. *IEEE Trans. Electron Devices* **2018**, *65*, 4102−4108.
(65) Wang, Z.; Li, Q.; Besenbacher, F.; Dong, M. Facile Synthesis of Single Crystal $PtSe_2$ Nanosheets for Nanoscale Electronics. *Adv. Mater.* **2016**, *28*, 10224−10229.
(66) Yang, Y.; Jang, S. K.; Choi, H.; Xu, J.; Lee, S. Homogeneous Platinum Diselenide Metal/Semiconductor Coplanar Structure Fabricated by Selective Thickness Control. *Nanoscale* **2019**, *11*, 21068−21073.


https://dx.doi.org/10.1021/acsami.0c00116
ACS Appl. Mater. Interfaces 2020, 12, 14341−14351